Measurement of the Band-to-Band Registration of the SNPP VIIRS Imaging System from On-Orbit Data

James C. Tilton, *Senior Member, IEEE*, Guoqing (Gary) Lin and Bin Tan

Abstract — **The Visible Infrared Imaging Radiometer Suite (VIIRS) instrument was launched 28 October 2011 onboard the Suomi National Polar-orbiting Partnership (SNPP) satellite. The VIIRS instrument is a whiskbroom system with 22 spectral and thermal bands split between 16 moderate resolution bands (M-bands), five imagery resolution bands (I-bands) and a day-night band. In this study we measure the along-scan and along-track band-to-band registration between the I-bands and M-bands from on-orbit data. This measurement is performed by computing the Normalized Mutual Information (NMI) between shifted image band pairs and finding the amount of shift required (if any) to produce the peak in NMI value. Subpixel accuracy is obtained by utilizing bicubic interpolation. The product of the NMI peak slope and the NMI peak value is shown to be a better criterion for evaluating the quality of the NMI result than just the NMI peak value. Registration shifts are found to be similar to pre-launch measurements and stable (within measurement error) over the instrument's first four years in orbit.**

Index Terms— **Satellite navigation systems, image registration, image analysis.**

I. INTRODUCTION

THE NASA/NOAA Visible Infrared Imaging Radiometer Suite (VIIRS) instrument onboard the Suomi National Polar-orbiting Partnership (SNPP) satellite was launched on 28 October 2011. A detailed description of this instrument and its early on-orbit performance is provided in [1]. VIIRS has 5 imagery resolution bands (bands I1 to I5) with 32 detectors each, 16 moderate resolution bands (bands M1 to M16) and a panchromatic day-night band (DNB) with 16 detectors each. The nominal spatial resolution is 375 m for I-bands and 750 m for M-bands and the DNB. In this study we measure the along-scan and along-track band-to-band registration between the I-bands and M-bands from on-orbit data.

Most early approaches to image matching were based on the cross-correlation method. For a general overview of image matching see [2]. However, the effectiveness of cross-correlation is diminished for spectral bands that appear quite different due to differences in spectral responses at different wavelengths. To overcome this problem we use the Normalized Mutual Information (NMI) method for image registration [3, 4, 5, 6]. The NMI method relies on the statistical dependency between two images to determine their correlation. Both positive and negative radiometric correlations between the images contribute positively to the statistical dependency between the images. In contrast, positive and negative radiometric correlations tend to cancel each other out in the cross-correlation method.

Wang, et al [7] recently reported on an approach for measuring the band-to-band registration (BBR) of VIIRS reflective solar bands based on lunar observations. This method depends on special lunar observations of limited availability. Besides being limited to the reflective solar bands, the results from this method must be carefully corrected for seasonal variations in the moon's appearance. Lin, et al [8] recently reported on an approach for measuring VIIRS BBR based on an on-orbit estimation of the shape and location of the line spread function from images of the Lake Pontchartrain Causeway Bridge. This approach was only effective for bands in which the contrast between the bridge and surrounding water was sufficiently strong. It also required some manual analysis steps.

Verification of an instrument's BBR is important because of the potential impacts BBR misregistration on the quality of science data products produced. For example, Xie, et al [9] perform a general impact analysis of MODIS BBR in which they conclude that "the influence of misregistration is small in the homogeneous or semi-homogeneous areas, but relatively large at the boundary areas."

In the following sections we provide a more detailed description of the imagery and moderate resolution band data obtained from the VIIRS instrument, and summary descriptions of Normalized Mutual Information (NMI) and bicubic interpolation. We then provide a detailed description of our band-to-band registration approach which is based on NMI and achieving subpixel accuracy using bicubic interpolation. We show that the product of the NMI peak slope and the NMI peak

value is a better criterion for evaluating the quality of the NMI result than just the NMI peak value. Finally, we provide selected detailed results and summary results for all VIIRS bands from which statistically robust results were obtained.

II. DESCRIPTION OF THE VIIRS IMAGERY AND MODERATE RESOLUTION BAND DATA

The VIIRS instrument collects data from 32 detectors for each of the five I-bands, and 16 detectors for each of the sixteen M-bands in each cross track scan. These detectors are rectangular with the smaller dimension in the along scan direction. A sample aggregation scheme is employed to equalize the along-scan size of the recorded image sample. In the zone from nadir out to ±31.72° three samples are averaged or aggregated along the scan direction, 31.72° to 44.86° out from nadir two samples are aggregated, and outwards from 44.86° no aggregation is employed. These three zones are called the "3x1 aggregation," "2x1 aggregation," and "no aggregation" zones, respectively. (The no aggregation zone is also sometimes called the "1x1 aggregation zone.") In the 3x1 aggregation zone the data from all 32 (16) detectors in each I-band (M-band) array are transmitted to the ground, whereas in the 2x1 aggregation zone the data from first two and last two (first and last) rows of each cross track scan are deleted before the data is transmitted to the ground, and in the no aggregation

zone the data from the first four and last four (first two and last two) rows of each cross track scan are deleted. This data deletion scheme is called "bow-tie deletion." These sample aggregation and bow-tie deletion schemes are unique to the VIIRS instrument. Table I summarizes the characteristics of the M-band data for the three aggregation zones, including range of horizontal sampling intervals (HSIs) in the scan and track directions.

The sample aggregation scheme affects the amount of along-scan BBR shift. Fig. 1 displays the pre-launch laboratory measurements of BBR versus band I1. From these measurements we can see that the BBR shifts are smallest in the 3x1 aggregation zone and largest in the no aggregation zone. The largest positive shift is seen between bands I1 and M11 and the largest negative shift is seen between bands I1 and M13.

III. NORMALIZED MUTUAL INFORMATION

We first describe the Mutual Information (MI) method for image registration and then show how Normalized Mutual Information (NMI) is related to MI.

In the MI method, the mutual dependence of a pair of images, considered as a pair of random variables, is measured by their mutual information. Formally, the mutual information of two discrete random variables X_f and X_s can be defined as:

TABLE I
CHARACTERISTICS OF THE THREE AGGREGATION ZONES FOR THE M-BANDS.

	3x1 Aggregation	2x1 Aggregation	No Aggregation
Scan Angle	-31.72° to 31.72°	- 44.86° to -31.72°, 31.72° to 44.86°	-56.28° to -44.86°, 44.86° to 56.28°
5-Min swath columns	1009 to 2192	641 to 1008 and 2193 to 2560	1 to 640 and 2561 to 3200
HSI_scan (m)	784 at 0°, 1178 at ±31.72°	785 to 1317	659 to 1706
HSI_track (m)	750 at 0°, 905 at ±31.72°	905 to 1138	1139 to 1655
Detectors data retained from	1-16	2-15	3-14

Note: For the I-bands, the column values and detector numbers are doubled, and the HSI resolutions are twice as fine as for the M-bands, since the I-bands are nested into the M-bands in a 2x2 scheme. The HSI values are for an orbit of 838.8km, which is the NPP satellite mean altitude as of this writing.
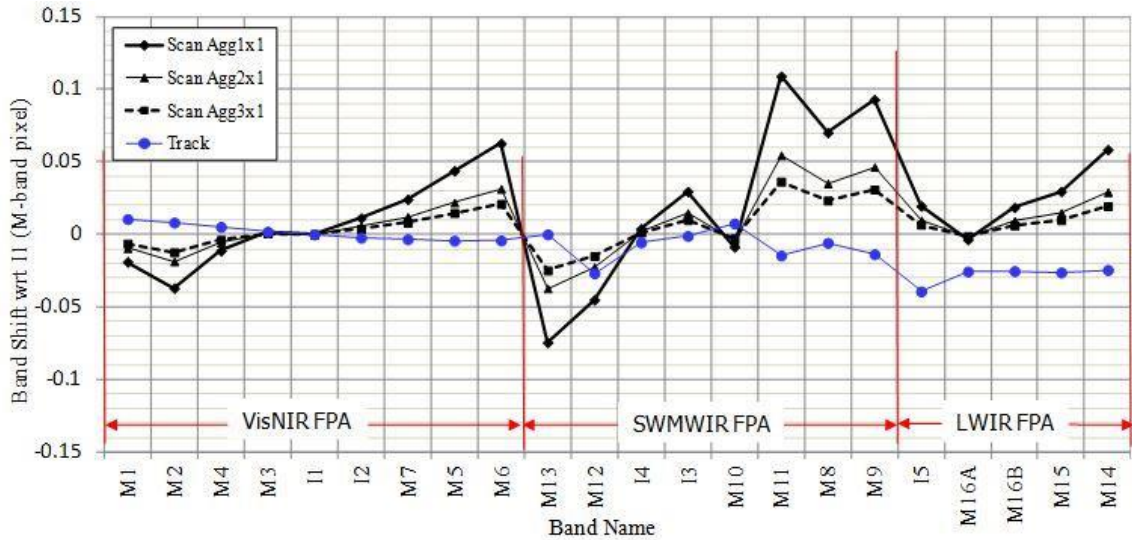

Fig. 1. Pre-launch band-to-band (BBR) measurements of the I-bands and M-band versus band I1. The bands are grouped by the focal plane array (FPA) on which the sensors are placed and listed in the order the sensors are placed on their FPA. There are three FPAs: visible and near infrared (VisNIR), shortwave and midwave infrared (SWMWIR) and long-wave infrared (LWIR). Band M16 is created by time delay integration from two sets of detectors (M16A and M16B).

$$MI(X_f; X_s) = \sum_{x_f \in X_f} \sum_{x_s \in X_s} p(x_f, x_s) \log\left(\frac{p(x_f, x_s)}{p(x_f)p(x_s)}\right), \quad (1)$$

where $p(x_f, x_s)$ is the joint probability density function of X_f and X_s, and $p(x_f)$ and $p(x_s)$ are the marginal probability density functions of X_f and X_s, respectively [3,10].

A pair of images, represented by the discrete random variables X_f and X_s, are considered best registered when the image represented by X_s is shifted to the location that maximizes the value of $MI(X_f; X_s)$. For practical implementation it is useful to reformulate MI in terms of entropy, defined as:

$$H(X) = -\sum_{x \in X} p(x) \log(p(x)). \quad (2)$$

Noting that $\log(ab) = \log(a) + \log(b)$ and $\log\left(\frac{a}{b}\right) = \log(a) - \log(b)$,

$$MI(X_f; X_s) = H(X_f) + H(X_s) - H(X_f, X_s). \quad (3)$$

To compute the mutual information, $MI(X_f; X_s)$, between two images we need to compute $H(X_f, X_s)$ - the joint entropy of X_f and X_s – and the marginal entropies - $H(X_f)$ and $H(X_s)$. Computing entropy requires the evaluation of $p(x_f, x_s)$ - the joint probability density function of X_f and X_s - and $p(x_f)$ and $p(x_s)$ - the marginal probability density functions of X_f and X_s, respectively. Probability entropy functions may be estimated from the histograms of an appropriately quantized image. We have found 6-bit quantization to be most effective for our application.

Here are the steps we use for computing MI:

1. Scale and quantize the images: To avoid potential problems with a small number of outlier values, we apply a 3σ filter to the image data. With 6-bit quantization, we linearly scale the data such that μ - 3σ (the mean value minus 3 times the standard deviation) corresponds to the value 1 and $\mu + 3\sigma$ corresponds to the value 64, clipping as necessary. The data is rounded to the nearest integer value. (The value "0" is reserved as a "no data" mask.) However, if a greater dynamic range is produced by linearly scaling the data such that the minimum value corresponds to 1 and the maximum value corresponds to 64, the scaling based on the minimum and maximum values is used instead.

2. Compute the joint histogram between the 6-bit quantized fixed and shifted images: Let J_{fs} be an array of size 64*64 initialized to zero. J_{fs} is accumulated by incrementing $J_{fs}[x_f + 64x_s]$ for each image pixel location at which the fixed and shift image pixel values are valid (x_f and x_s are the quantized fixed and shift image pixel values).

3. Compute the joint probability density function, p_{fs}, by dividing $J_{fs}[x_f + 64x_s]$ by the total number of valid pixels.

4. Compute the joint entropy:

$$H(X_f, X_s) = -\sum_{p_{fs} > 0} p_{fs} \log(p_{fs}) \quad (4)$$

5. Compute the marginal probability density functions:

$$p_f(k) = \sum_{l=1}^{63} p_{fs}(k + 64l), \text{ and}$$
$$p_s(l) = \sum_{k=1}^{63} p_{fs}(k + 64l). \quad (5)$$

6. Compute the marginal entropies:

$$H(X_f) = -\sum_{p_f > 0} p_f \log(p_f), \text{ and}$$
$$H(X_s) = -\sum_{p_s > 0} p_s \log(p_s). \quad (6)$$

7. Finally, compute the mutual information value:

$$MI(X_f; X_s) = H(X_f) + H(X_s) - H(X_f, X_s). \quad (7)$$

Normalized Mutual Information (NMI) is defined as the mutual information divided by the joint entropy:

$$NMI(X_f; X_s) = MI(X_f; X_s)/H(X_f, X_s)$$
$$= [H(X_f) + H(X_s) - H(X_f, X_s)]/H(X_f, X_s)$$
$$= [H(X_f) + H(X_s)]/H(X_f, X_s) - 1. \quad (8)$$

NMI has a nominal range of 0 to 1. An NMI value of 0 corresponds to 0% dependence (i.e., full independence) of the compared images, whereas a value of 1 corresponds to 100% or complete dependence between the images.

Studholme, et al [11] assert that NMI performs better than MI in cases where the overlap region between the compared images is small. However, in the cases we are dealing with, the overlap region between our compared images is relatively large because the amount of shifts we observe are very small (a fraction of a pixel). Thus, we should see very little difference in performance between NMI and MI. However, using a fixed threshold with NMI is more meaningful because of its known range.

IV. BICUBIC INTERPOLATION FOR SUB-PIXEL ACCURACY

We utilize bicubic interpolation to obtain sub-pixel accuracy for our BBR measurements. Our implementation of bicubic interpolation is based on Kenneth Joy's [12] summary description of the Catmull-Rom splines [13]. A cubic curve can be represented parametrically by the polynomial function:

$$P(t) = a_0 + a_1 t + a_2 t^2 + a_3 t^3 \quad (9a)$$

that has the first derivative (slope):

$$P'(t) = a_1 + 2a_2 t + 3a_3 t^2. \quad (9b)$$

An interpolated curve for t in the range of 0 to 1 can be specified by setting the values of P(0), P(1), P'(0) and P'(1) and solving the resulting system of equations:

$$P(0) = a_0$$
$$P(1) = a_0 + a_1 + a_2 + a_3$$
$$P'(0) = a_1$$
$$P'(1) = a_1 + 2a_2 + 3a_3. \quad (10)$$

We would like to fit an interpolative curve passing through $n + 1$ control points $\{P_0, P_1, …, P_n\}$. We define this interpolative curve for the segment P_i to P_{i+1} by using these two control points and also specifying the tangent to the curve at each of these control points to be

$$\frac{P_{i+1} - P_{i-1}}{2} \text{ and } \frac{P_{i+2} - P_i}{2} \quad (11)$$

respectively.

Several algebraic steps lead to the following matrix equation for the interpolative curve P(t) for each line segment P_i to P_{i+1}:

$$P(t) = [1 \ t \ t^2 \ t^3] M \begin{bmatrix} P_{i-1} \\ P_i \\ P_{i+1} \\ P_{i+2} \end{bmatrix} \qquad (12a)$$

where

$$M = \frac{1}{2} \begin{bmatrix} 0 & 2 & 0 & 0 \\ -1 & 0 & 1 & 0 \\ 2 & -5 & 4 & -1 \\ -1 & 3 & -3 & 1 \end{bmatrix} \qquad (12b)$$

See Joy [12] for the details. Note that the curve is undefined for the line segments P_0 to P_1 and P_{n-1} to P_n since one of the two tangents is not defined for those line segments.

Bicubic interpolation is the extension of the above cubic interpolation for a single dimensional curve to a two-dimensional image. This extension is accomplished by first performing the cubic interpolation along the column dimension and then applying the cubic interpolation along the row dimension.

V. OUR APPROACH TO MEASURING BBR

Since the VIIRS image data is collected in 32 row scans (16 row for M-bands), we designed our BBR measurement approach around analyzing 32 (or 16) row scan chips. Instead of using square chips with 32 (or 16) columns, we used rectangular scan chips with the number of columns twice the number of rows. We did this to give us better correlation resolution in the along scan direction.

In evaluating the band-to-band registration between two VIIRS radiance images, we designate one radiance image as the "fixed" image and the other radiance image as the "shift" image. For programming convenience, we adopt the convention that if the fixed image is an I-band image, the shift image must also be an I-band image. When comparing I-band images to M-band images, the M-band image is always the fixed image and the I-band image is always the shift image.

We performed an initial screening of our scan chips for clouds and water. While our BBR approach will work in the presence of clouds and water, we decided it would be best to screen out scan chips that have more than 5% clouds and 75% water. We felt more comfortable making our results depend on fixed land features, or land/water boundary features, instead of potentially highly variable cloud features.

To perform the cloud screening we extracted a binary cloud mask from the 5-Min L2 Swath Cloud Mask data by selecting as cloud pixels those flagged as having medium or high cloud mask quality and flagged as being probably or confident cloudy. Since the Cloud Mask is not computed for all data lines, we filled in the gaps for our cloud mask by copying the value from the nearest line where the Cloud Mask was computed. Fig. 3 shows an example of the resulting binary cloud mask for a VIIRS image from over the Mediterranean Sea collected on July 31, 2013. An RGB representation of this VIIRS image is shown in Fig. 2.

To perform water screening, we extracted a binary water mask from the 5-Min L2 Swath Surface Type data by selecting the Water Bodies surface type (surface type number 17). Again,

since the Surface Type is not designated for all data lines, we filled the gaps for our water mask by copying the value from the nearest line where the Surface Type was designated. The resulting binary water mask for the Mediterranean Sea data set is displayed in Fig 4.

In our initial screening of the data, for each cross track scan, we divide the data up into non-overlapping scan chips as described in the previous paragraph. While we will eventually perform NMI analysis on the data interpolated to 40 times the

Fig. 2. Imagery Resolution 5-Min L1 Swath Radiance data (bands I4, I3 and I2 shown as red, green and blue, respectively, with histogram equalization enhancement) for a VIIRS image from over the Mediterranean Sea collected on July 31, 2013. (Note: Since this image was acquired from an ascending orbit, the southeast corner is at the top-left corner as displayed.)
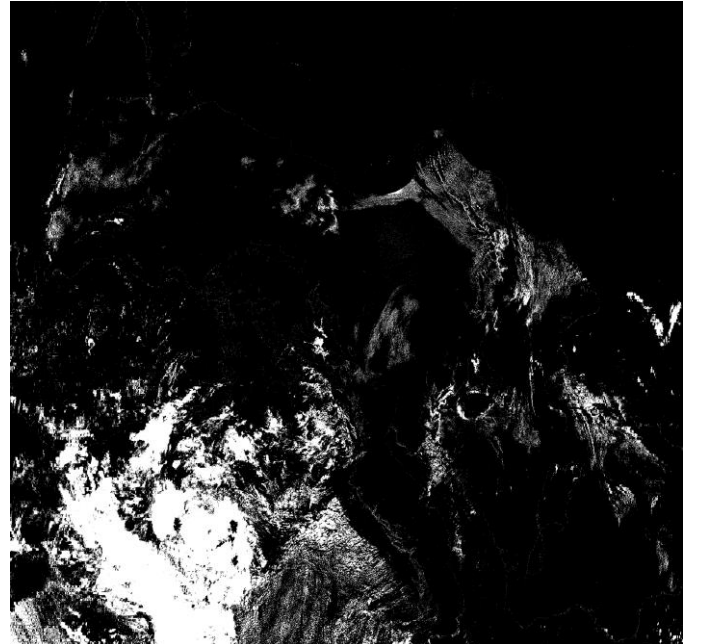

Fig. 3. Cloud mask extracted from the 5-Min L2 Swath Cloud Mask data for a VIIRS image from over the Mediterranean Sea collected on July 31, 2103 (cloud areas are colored white).
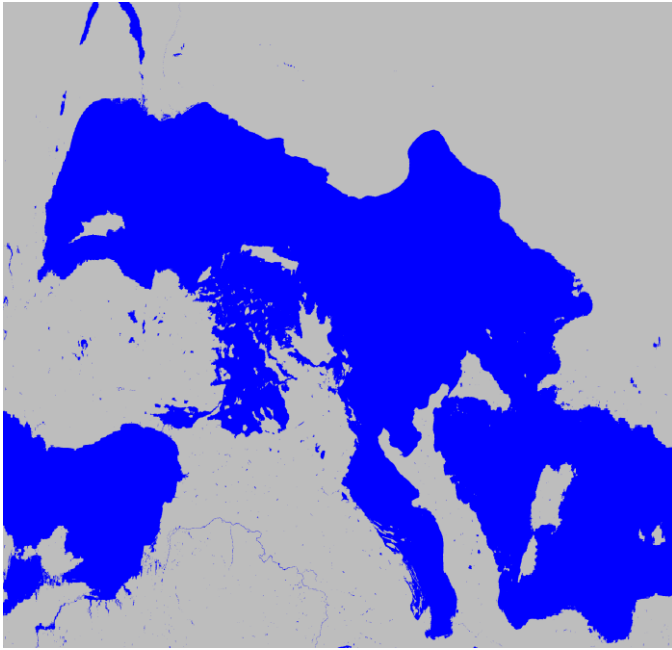
Fig. 4. Water mask extracted from the 5-Min L2 Swath Surface Type data for a VIIRS image from over the Mediterranean Sea collected on July 31, 2103 (water areas are colored blue).

original spatial resolution, to reduce processing time, we perform our initial screening on data interpolated to 4 times the original spatial resolution. (When we compare I-band data to M-band data, the I-band data is interpolated to 4 times the original spatial resolution and the M-band data is interpolated to 8 times the original spatial resolution.) In our experiments we found that we had to interpolate the data to at least 4 times the original spatial resolution to obtain a reliable prediction of the NMI peak value at 40 times the original spatial resolution.

For each of the non-overlapping scan chips we calculate the zero shift NMI for scan chips with less that 5% cloud pixels and less than 75% water pixels. For scan chips with zero shift NMI >= 0.10, we also calculate the zero shift NMI for four additional scan chips in the vicinity (if the cloud and water percentage thresholds are satisfied). For a scan chip with of column width C_w, and scan chip starting column of C_s, these four additional scan chips have starting columns $C_s - C_w/2$, $C_s - C_w/4$, $C_s + C_w/4$, and $C_s + C_w/2$.

For each cross track scan in which at least one scan chip is found to have zero shift NMI of at least 0.10, we find the scan chip with the largest zero shift NMI, and find the peak NMI by shifting the shift image locally. In doing this we also compute "minimum peak slope" and the "eccentricity" for the peak. The minimum peak slope is the minimum of the cross track, cross scan and diagonal slopes from the NMI peak. The eccentricity is cross track slope from the NMI peak divided by the cross scan slope from the NMI peak. If this ratio is less than one, the eccentricity is instead the inverse of this value. A scan chip is retained for further consideration if the peak NMI is at least 0.10, the minimum peak slope is at least 0.035, and the eccentricity is no more than 1.25. Scan chips with low peak NMI and low minimum peak slope are eliminated due to weak correlation between the compared chips. Scan chips with high

eccentricity are eliminated from further consideration to ensure that the cross track and along track shift determinations will have similar validity in each direction.

This screening continues for each cross track scan until 10 non-overlapping scan chips are retained from the cross track scan or no more scan chips are found to satisfy the screening criteria. As this screening proceeds through the rest of the cross track scans, up to 100 scan chips with the highest peak NMI are retained for further consideration.

After up to 100 "best" scan chips are identified by the above described screening process, we perform a fine resolution NMI analysis to find the along track and row shifts for each selected scan chip at 40 times the original resolution using bicubic interpolation for each data set. (In the case of comparing an M-band to an I-band, the M-band is interpolated to 40 times the original resolution and the I-band is interpolated to 20 times the original resolution.) The peak NMI, minimum peak slope and eccentricity are calculated along with the along scan and along track shifts.

We will eventually select a set of "best" measurements across several data sets to compute a "best estimate" of the along scan and along track shifts. We used the peak NMI value as the primary criterion in our initial tests. However, our experiments showed us that a better final selection criterion is the product of the peak NMI with the minimum peak slope. The standard deviation of our along scan and along track shifts using the product criterion was generally found to be about 50 to 75% of the standard deviation of our estimates using just the peak NMI value as our criterion. (See our discussion of results.)

So after we compute our fine resolution NMI results, we record to a log file peak NMI, minimum peak slope, eccentricity and along scan and along track shifts for all scan chips that still meet the previous eccentricity threshold and that also meet a new threshold of the product of the NMI peak times minimum peak slope no less than 0.0035 (=0.10x0.035). Not all of the best scan chips found through the screening process will necessarily meet these revised threshold requirements.

The results of this best scan chip selection process is displayed in Fig. 5 for the bands I3 versus I4 for the July 31, 2013 VIIRS image displayed in Fig. 2. Note that most of the scan chips are found along shore lines.

VI. COMBINED ANALYSIS OF BBR MEASUREMENTS

We performed a combined analysis on a set of 34 relatively cloud free VIIRS data sets. These data sets were chosen from geographic areas that have numerous contrasting shoreline features from seas, bays or lakes. These data sets, which are listed in Table II, were obtained through the Level 1 and Atmosphere Archive and Distribution System web site (LAADS Web) (http://ladsweb.nascom.nasa.gov) in the form of level 1 (L1) 5-minute swath data. Data from Archive Set AS3110 (archive set 3110) was used in this study (products produced by the C1.1 reprocessing of VIIRS instrument data at NASA's Suomi NPP Land Science Investigator-led Process System (SIPS)).

In our combined analysis procedure we considered each band pair in turn. For each band pair we accumulated the best results
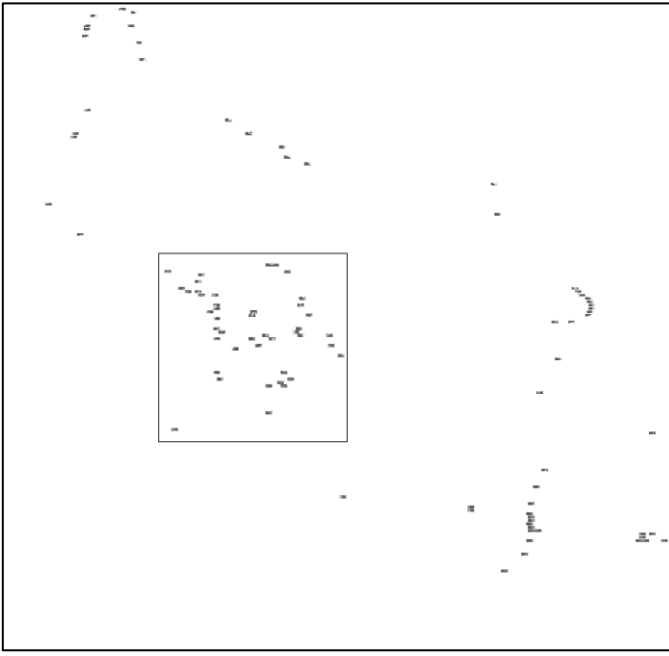
(a)
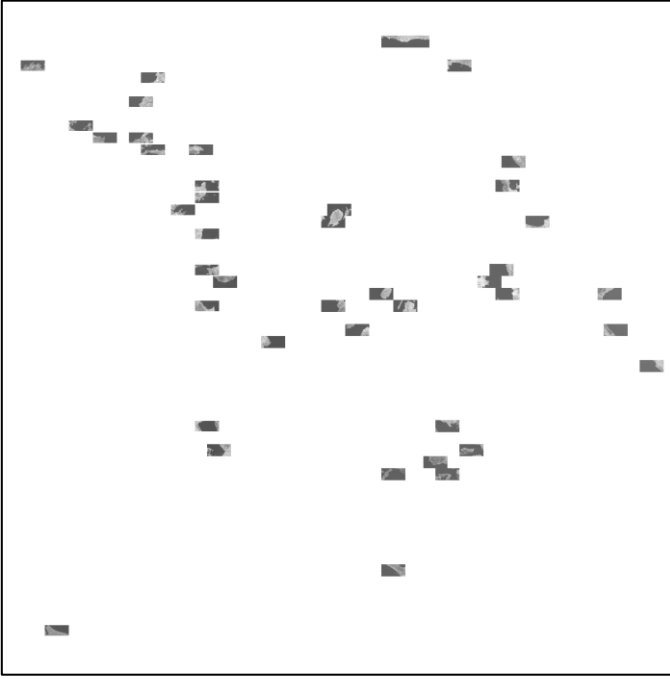
(b)

Fig. 5. (a) The 100 "best" scan chips selected from the July 31, 2013 VIIRS image from over the Mediterranean Sea for the comparison between I-bands 3 and 4 (band I4 is displayed). (b) Magnified section from the portion outlined in (a).

TABLE II
DATA SETS ANALYZED.

yyyyddd.hhmm*	Date	Location
2012065.1835	5 Mar 2012	Great Lakes, North America
2012192.1715	10 Jul 2012	Great Lakes, North America
2012192.1855	10 Jul 2012	Great Lakes, North America
2012207.1045	25 Jul 2012	Black & Mediterranean Seas
2012244.1050	31 Aug 2012	Black & Mediterranean Seas
2012254.1105	10 Sep 2012	Black & Mediterranean Seas
2013153.1125	2 Jun 2013	Lake Victoria, Africa
2013157.1150	6 Jun 2013	Lake Victoria, Africa
2013173.1150	22 Jun 2013	Lake Victoria, Africa
2013178.1155	27 Jun 2013	Lake Victoria, Africa
2013179.1010	28 Jun 2013	Black & Caspian Seas
2013193.1735	12 Jul 2013	Great Lakes, North America
2013194.1155	13 Jul 2013	Lake Victoria, Africa
2013205.1150	24 Jul 2013	Lake Victoria, Africa
2013212.1130	31 Jul 2013	Black & Mediterranean Seas
2013222.1005	10 Aug 2013	Black & Caspian Seas
2013235.0920	23 Aug 2013	Black & Caspian Seas
2013240.1105	28 Aug 2013	Black & Mediterranean Seas
2013269.1850	26 Sep 2013	Great Lakes, North America
2014137.0920	17 May 2014	Black & Caspian Seas
2014176.1720	25 Jun 2014	Hudson Bay, North America
2014176.1900	25 Jun 2014	Hudson Bay, North America
2014178.1820	27 Jun 2014	Great Lakes, North America
2014192.0855	11 Jul 2014	Northern Europe
2014213.1035	1 Aug 2014	Black & Mediterranean Seas
2014239.1050	27 Aug 2014	Black & Mediterranean Seas
2014245.0855	2 Sep 2014	Black & Caspian Seas
2015192.1110	11 Jul 2015	Lake Victoria, Africa
2015196.1135	15 Jul 2015	Lake Victoria, Africa
2015204.1100	23 Jul 2015	Black & Mediterranean Seas
2015209.1750	28 Jul 2015	Great Lakes, North America
2015222.1020	10 Aug 2015	Black & Caspian Seas
2015229.1115	17 Aug 2015	Lake Victoria, Africa
2015230.1115	18 Aug 2015	Northern Europe

* Year (yyyy), day of year (ddd), start hour (hh) and minute (mm).

product of NMI peak times minimum peak slope in each aggregation zone. For those band pairs for which we found at least 50 results with this product no less than the threshold of 0.0035, we computed the mean and standard deviation of the along track and along scan shifts in each aggregation zone.

The product of our analysis is a set of tables that list the along scan and along track shifts for each aggregation zone, and the along track shift across all aggregation zones for all band combinations. The detailed results of these seven cases of the 210 combinations of band pairs are too numerous to present in a paper. However, we provide a summary presentation and discussion of the results in the next section.

VII. DISCUSSION OF COMBINED ANALYSIS RESULTS

In a previous section we noted that the product of the peak NMI with the minimum peak slope was found to be a better selection criterion than the peak NMI value itself. We noted that the standard deviation of our along scan and along track shifts using the product criterion was generally found to be less than the standard deviation of our estimates using just the peak NMI value as our criterion. This effect is demonstrated in the plots of mean along scan and along track shifts versus standard deviation displayed in Figs. 6 and 7. These plots clearly show that when the samples are selected based on the product

across all data sets and selected up to 100 results with the highest product of NMI peak times minimum peak slope. For those band pairs for which we found at least 50 results with this product no less than the threshold of 0.0035, we computed the mean and standard deviation of the along track shift across all aggregation zones. We also then segregated the data by aggregation zone and selected up to 100 results with the highest

criterion, the standard deviation of the shift results is roughly 50-75% of what is obtained when the samples are selected based on the minimum MI peak value alone.

Fig. 7 shows that for the bulk of the measurements in all but the 1x1 aggregation zone, the standard deviation of the measurements is under about 0.07. For those measurements with higher standard deviation, the standard deviation can be reduced by removing outliers from the calculations. We modified our combined analysis procedure to incrementally remove outliers until the standard deviation is under a specified threshold value or until no fewer than 50 measurements remain. In order to perform some measure of outlier elimination in each aggregation zone, we chose to use a standard deviation threshold of 0.06.

In Fig. 8 we plot the mean along scan and along track shift results that we consider to be valid after outlier elimination. We consider valid the band versus band combinations where we found at least 50 scan chips out of all data sets with product criterion meeting the 0.0035 threshold value. In all but the no aggregation zone, we observe that the mean shift values are all generally less than 0.06 pixel (M-band HSI). However, in the 1x1 aggregation zone, the along scan shifts are about twice as large, ranging from -0.102 pixel (for fixed band M13 and shift band I2) to 0.121 pixel (for fixed band M6 and shift band M13). This is consistent with the pre-launch BBR measurements (see Fig. 1). We also note that the outlier elimination process did not affect the overall spread of the mean shift values.

For some band pair combinations we did not find at least 50 scan chips meeting our quality criteria in some or all of the aggregation zones. This problem was most prevalent in the no aggregation zone. Table III lists those band pairs for which fewer than 50 valid BBR measurements were found in the no aggregation zone. Most of these band pairs involve a comparison between band M9 and another band. The worst case was the attempt at measuring the BBR between band M9 and band I4, where only 3 valid measurements were found for the mean column shift in the 3x1 aggregation zone, only 1 valid

measurement was found for the mean column shift in the 2x1 aggregation zone, no valid measurements were found for the mean column shift in the no aggregation zone and only 4 valid measurements were found for the mean row shift across all aggregation zones. Less than 50 valid chips were found for comparisons between band M9 and bands M6, M13, I1, I2, I3 and I4 in all cases. However, at least 50 valid chips were found for all cases of comparisons between band M9 and bands M1, M2, M3, M4, M14, M15 and M16. This problem with band M9 is due to the low contrast generally observed with data in this band.

In Fig. 1 we presented a plot of pre-launch measurements of BBR of all bands versus band I1. In Fig. 9 we provide plots comparing the pre-launch measurements with our on-orbit measurements. Note that plot values are missing for band M9 vs I1 due to an insufficient number of valid measurements. Note also that, for convenience, we plot our measured band M16 versus the on-lab measurement for band M16B (Band M16 is created by time delay integration of two sets of detectors: M16A and M16B). We generally see a good correspondence between the on-orbit and pre-launch measurements, with most of lab measurements falling well within the one standard deviation error bars of the on-orbit measurements. The only exceptions to this are for along scan shifts for bands M11 and I5 in the no aggregation zone (Agg 1x1) where the on-orbit measurements of the shifts are less than the pre-launch laboratory measurements.

VIII. TREND ANALYSIS

The 34 VIIRS data sets analyzed in the previous section are spread out in time over the instrument's first four years in orbit. We assumed in the previous section that the BBR was stable over those four years. We now check that assumption using band pairs that have relatively high products of NMI peak and NMI minimum peak slope values. We selected pairs of bands across the three focal plane assemblies (FPAs): Bands M3, M5 and M7 in the visible and near infrared (VisNIR) FPA, bands M8, M10 and M12 in the short-wave and mid-wave infrared (SWMWIR) FPA and bands M14, M15 and M16 in the long-wave infrared (LWIR) FPA. We compared both within and between FPAs, with the exception of between the VisNIR and LWIR FPAs, where we could not find a band pair providing high product values. For the within FPA comparisons we attempted to choose band pairs that were physically widely separated, but were limited in doing this to those band pairs that had high product values. Table IV lists the minimum peak product value for the band pairs selected for trend analysis.

TABLE III
BAND PAIRS WITH LESS THAN 50 VALID BBR
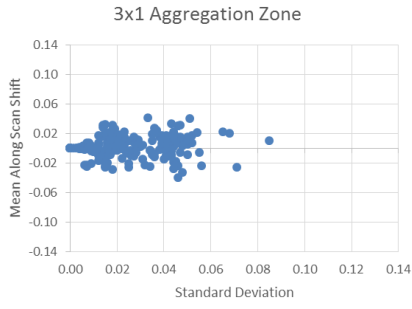MEASUREMENTS IN THE NO AGGREGATION ZONE.

Fixed image	Shift image	Number of Valid BBR Measurements			
		3x1 agg. zone	2x1 agg. zone	no agg zone	Combined
M1	M6	100	88	41	100
M4	M9	100	100	47	100
M5	M9	100	100	30	100
M6	M9	23	9	0	32
M7	M9	56	48	3	100
M8	M9	38	49	2	89
M9	M10	69	32	1	100
M9	M11	100	100	7	100
M9	M12	85	27	0	100
M9	M13	13	13	4	29
M1	I5	100	89	48	92
M9	I1	28	20	1	49
M9	I2	12	3	0	15
M9	I3	10	4	0	14
M9	I4	3	1	0	4
M9	I5	79	61	16	100

TABLE IV
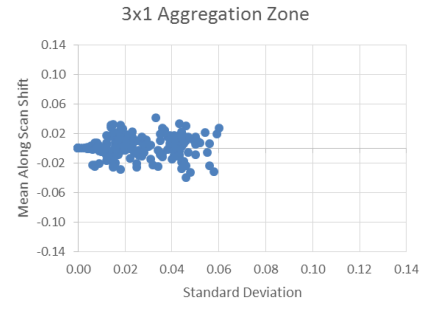BAND PAIRS CHOSEN FOR TREND ANALYSIS

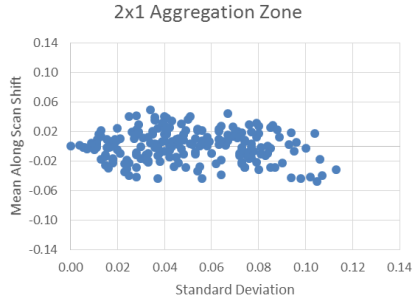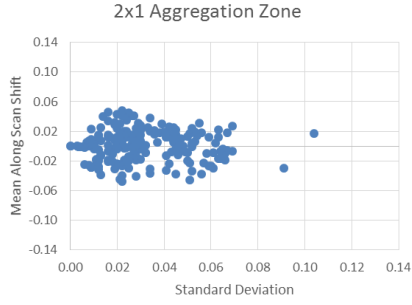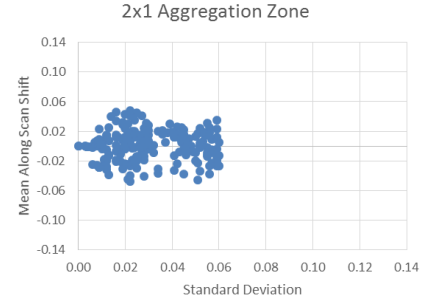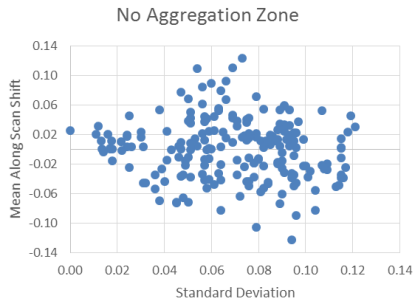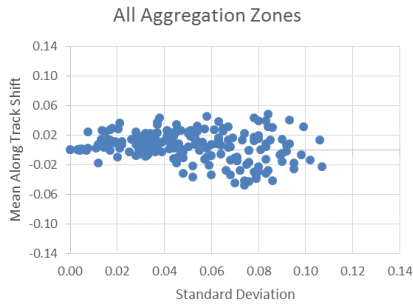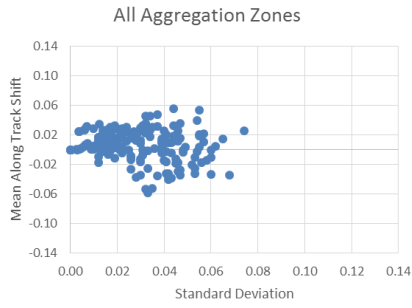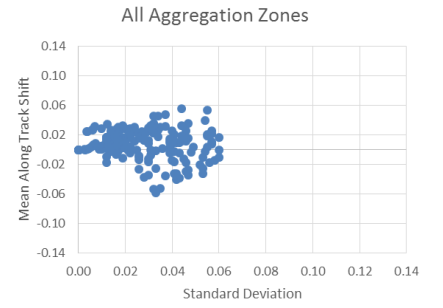| Fixed image	Shift image	Minimum Peak Product			
		3x1 agg. zone	2x1 agg. zone	no agg zone	Combined
M3	M5	0.67	0.63	0.15	0.80
M7	M8	0.57	0.48	0.49	0.61
M8	M10	0.45	0.40	0.35	0.50
M12	M15	0.50	0.42	0.23	0.51
M14	M16	0.92	0.75	0.46	0.92
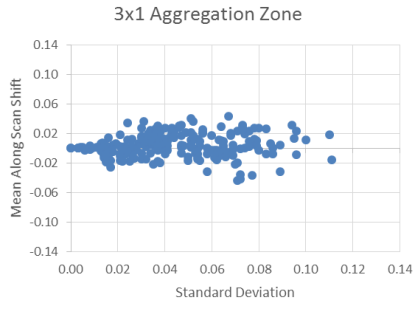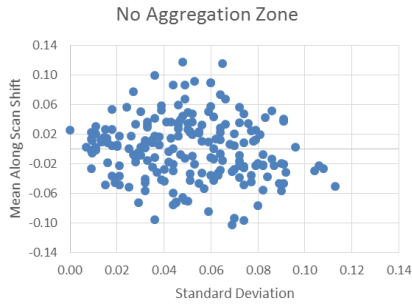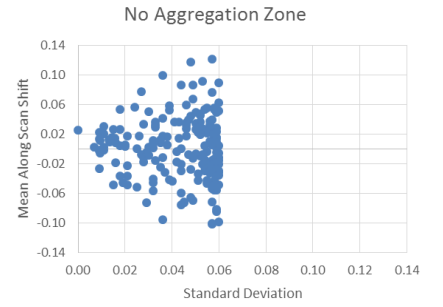
Fig. 6. Plots of the mean shifts for each band pair versus standard deviation in the different aggregation zone cases where the best measurements were selected using the MI peak criterion.

Fig. 7. Plots of the mean shifts for each band pair versus standard deviation in the different aggregation zone cases where the best measurements were selected using the MI peak times MI peak slope product criterion. Note that the standard deviation values are roughly 50-75% of those plotted in Fig. 6, indicating the superiority of the product criterion.

Fig. 8. Plots of the mean shifts for each band pair versus standard deviation in the different aggregation zone cases where the best measurements were selected using the MI peak times MI peak slope product criterion with incremental removal of outliers using a standard deviation threshold of 0.06. The outlier reduction process improves the reliability of the measurement without a noticeable change in overall mean shift values.
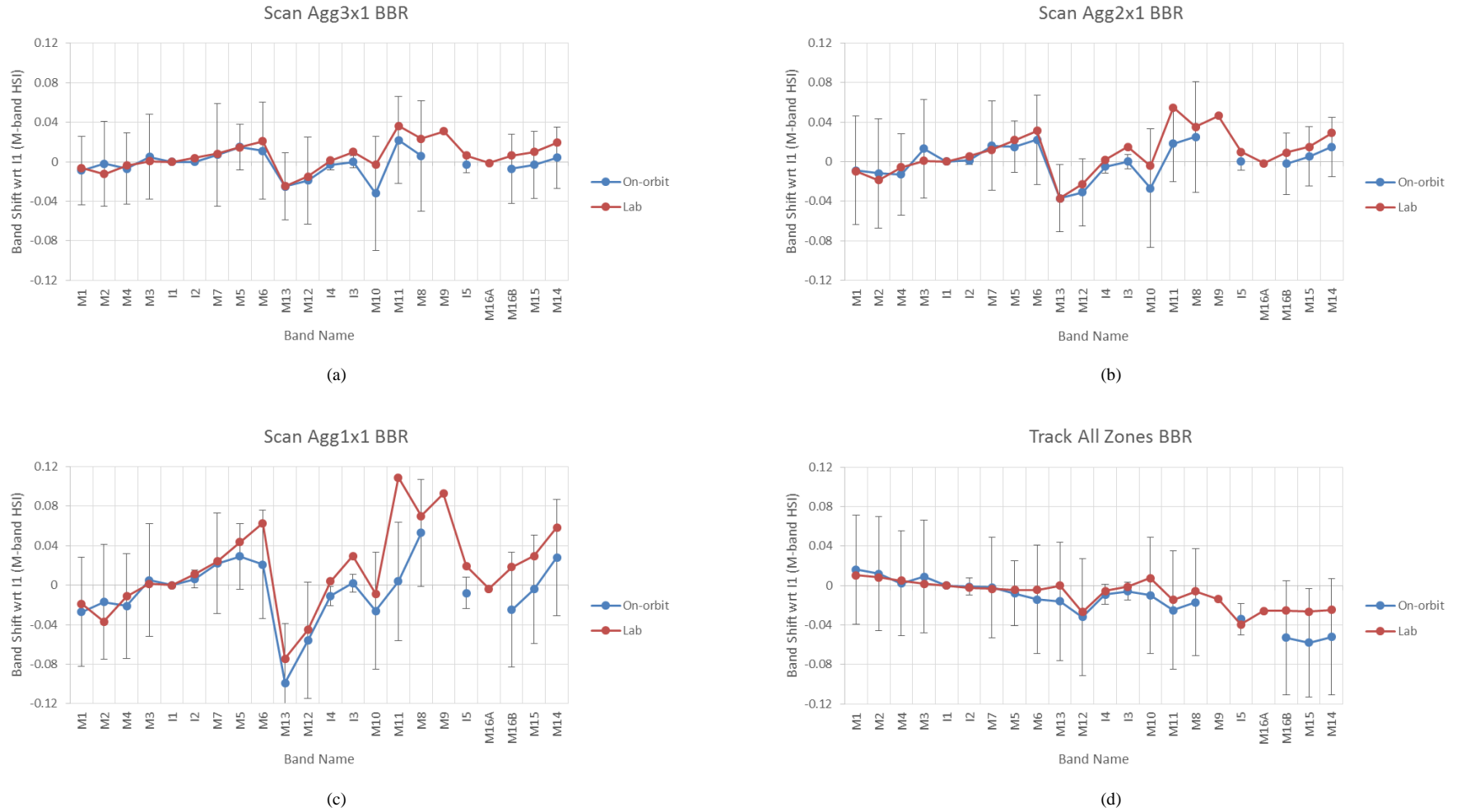
Fig. 9. Plots of pre-launch (lab) and on-orbit measured BBR shifts for all bands versus band I1. One standard deviation error bars are included with the on-orbit measurements. (a) Along scan shifts in the 3x1 aggregation zone. (b) Along scan shifts in the 2x1 aggregation zone. (c) Along scan shifts in the no aggregation zone. (d) Along track shifts across all aggregation zones.

Figs. 10-14 display the trend plots for the chosen band pairs. Included in the plots are dates on which at least 10 measurements were found to meet the minimum quality criteria. The most varied plots are for the comparison of bands M3 to M5 and bands M12 toM15 in the no aggregation zone, which corresponds to the cases with the smallest minimum peak product of all the cases listed in Table IV. With such a low minimum peak product value we should not trust the quality of the trend plot for these cases. However, all other trend plots indicate that the BBR was stable within measurement error (one standard deviation error bars are plotted) over the first four years of operation.

IX. CONCLUDING REMARKS

In this paper we have described an approach based on Normalized Mutual Information (NMI) for measuring band-to-band registration (BBR) between spectral bands with differing spectral characteristics. We also described how to obtain sub-pixel BBR measurement accuracy by using bicubic interpolation, and showed the product of the NMI peak slope and the NMI peak value to be a better criterion for evaluating the quality of the NMI result than just the NMI peak value. Through a combined analysis of 34 relatively cloud free VIIRS data sets taken from the first four years of service, we obtained good quality BBR measurements for all but 16 of the possible 210 band pair combinations. These BBR are generally in close agreement with pre-launch BBR measurements performed in a laboratory. Utilizing band pairs w1ith particular strong NMI correlations, we showed that the BBR of the VIIRS instrument has been stable (within measurement error) over its first four years in orbit.

REFERENCES

[1] C. Cao, F. J. De Luccia, X. Xiong, and F. Weng, "Early on-orbit performance of the visible infrared imaging radiometer suite onboard the Suomi National Polar-Orbiting Partnership (S-NPP) satellite," *IEEE Trans. Geosci. Remote Sens.*, vol. 52, no. 2, pp. 1142-1156, 2014.

[2] A. Gruen, "Development and Status of Image Matching in Photogrammetry," *The Photogrammetric Record*, vol. 27, pp. 36-57, 2012.

[3] A. A. Cole-Rhodes and P. K. Varshney, "Image registration using mutual information," in *Image Registration for Remote Sensing*, J. Le Moigne, N. S. Netanyahu and R. D. Eastman, eds, Cambridge: Cambridge University Press, pp. 131-149, 2011.

[4] H. M. Chen, P. K. Varshney, and M. K. Arora, "Performance of mutual information similarity registration of multitemporal remote sensing images," *IEEE Trans. Geosci. Remote Sens.*, vol. 41, no. 11, pp. 2445-2454, 2003.

[5] H. M. Chen, P. K. Varshney, and M. K. Arora, "Mutual information based image registration for remote sensing data," *Int'l Journal of Remote Sens.*, vol. 24, no. 18, pp. 3701-3706, 2003.

[6] K. Johnson, A. A. Cole-Rhodes, I. Zavorin and J. Le Moigne, "Mutual information as a similarity measure for remote sensing image registration," in *Proceedings of the SPIE Conference on Geo-Spatial Image and Data Exploitation II*, Orlando, FL, Vol. 4032, pp. 1072-1080, 2001.

[7] Z. Wang, X Xiong and Y. Li, "Improved Band-to-Band Registration Characterization for VIIRS Reflective Solar Bands Based on Lunar Observations," *Remote Sensing*, vol. 8, no.27, pp. 1-12, 2016.

[8] G. Lin, J. C. Tilton, R. E. Wolfe, K. P. Tewari, and M. Nishihama, "SNPP VIIRS spectral bands co-registration and spatial response characterization," in *Proc. SPIE*, 2013, 8866, Art. ID. 88661G.
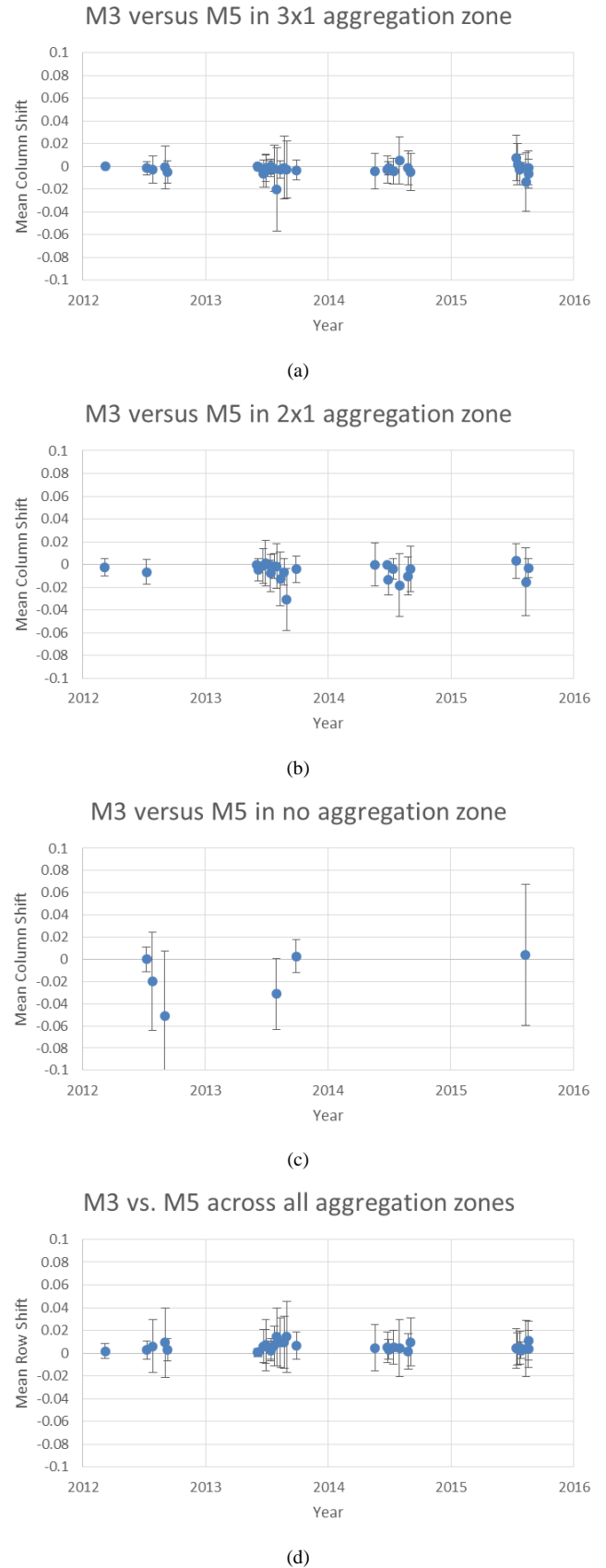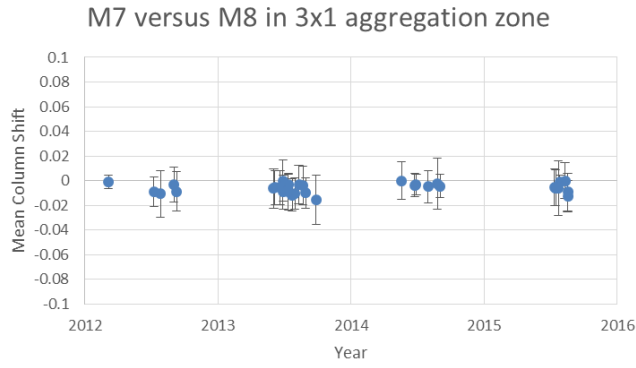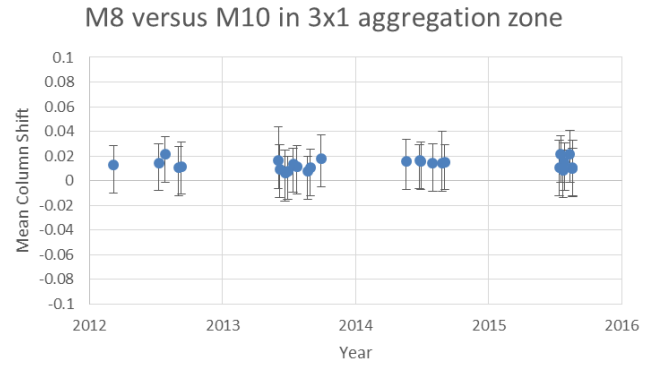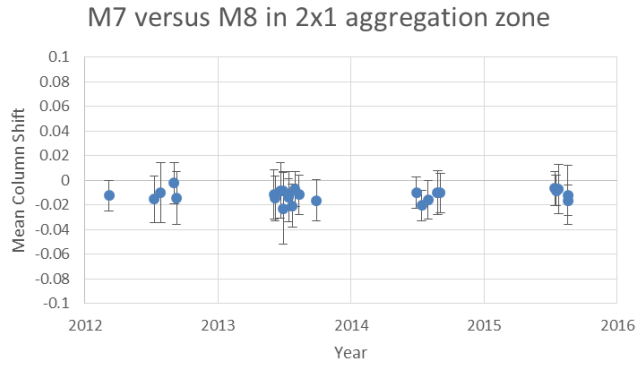
Fig. 10. Trend plots for the on-orbit measured mean column shifts for the 3x1, 2x1 and no aggregation zones and for the on-orbit measures mean row shifts across all aggregation zones for bands M3 versus M5.
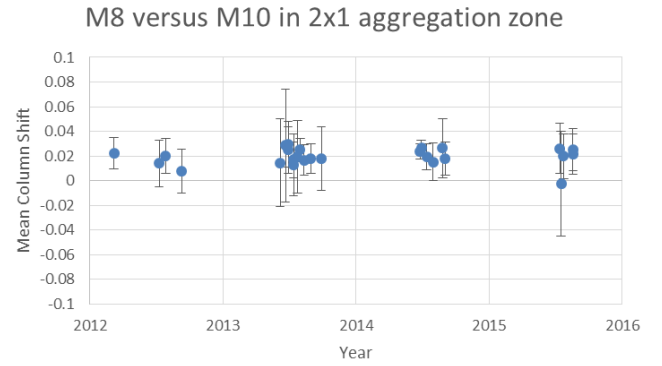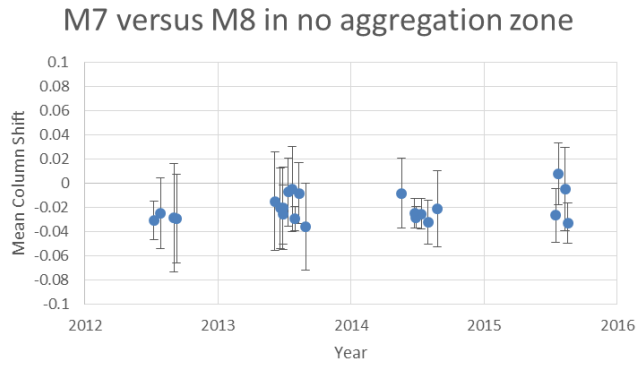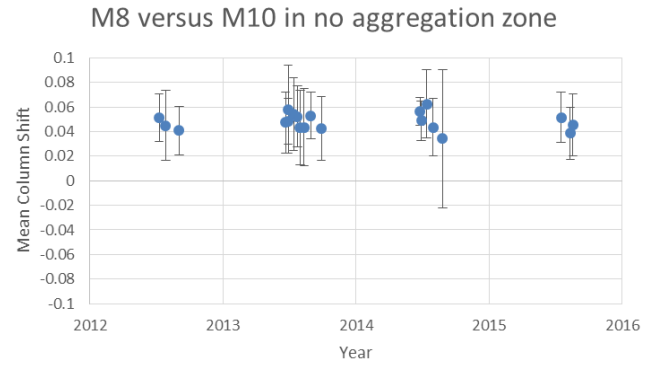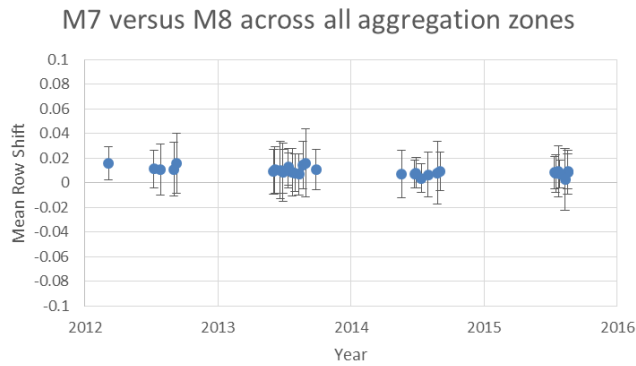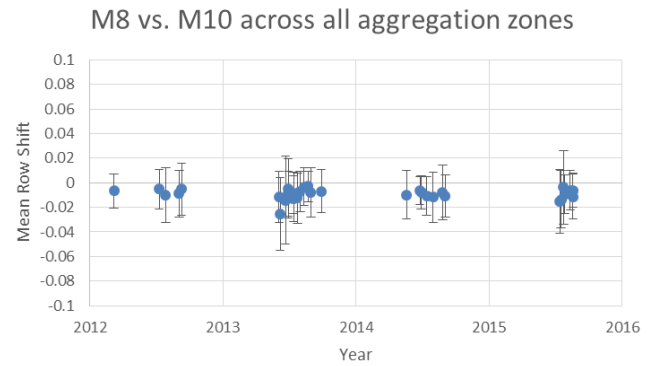
(a)

M7 versus M8 in 3x1 aggregation zone

(b)

M7 versus M8 in 2x1 aggregation zone

(c)

M7 versus M8 in no aggregation zone

(d)

M7 versus M8 across all aggregation zones

Fig. 11. Trend plots for the on-orbit measured mean column shifts for the 3x1, 2x1 and no aggregation zones and for the on-orbit measure mean row shifts across all aggregation zones for bands M7 versus M8.
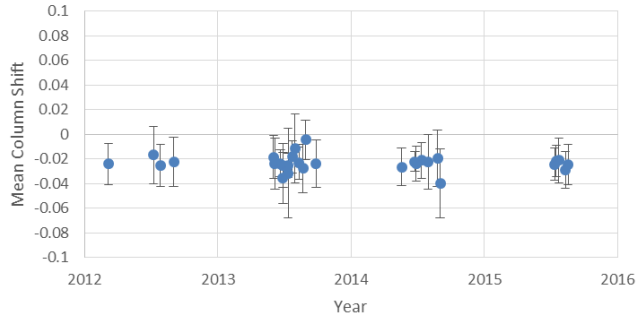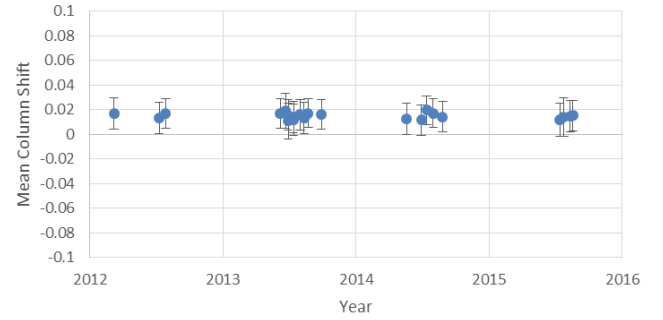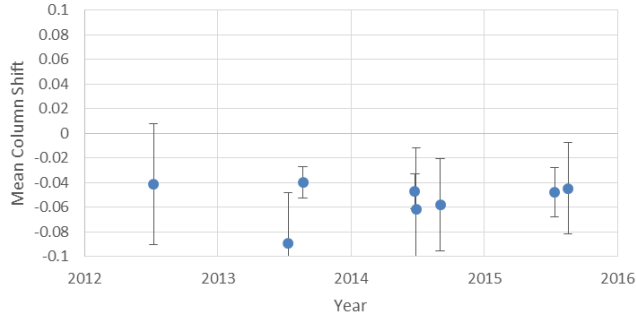

(a)

M8 versus M10 in 3x1 aggregation zone

(b)

M8 versus M10 in 2x1 aggregation zone

(c)

M8 versus M10 in no aggregation zone

(d)

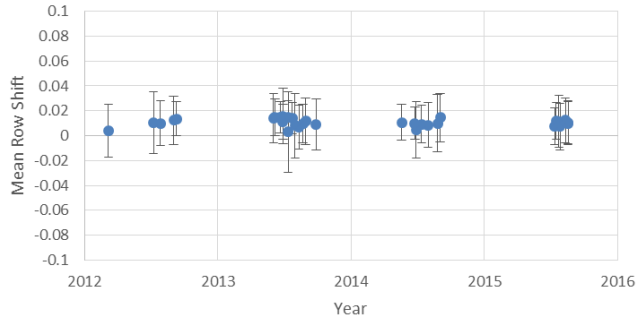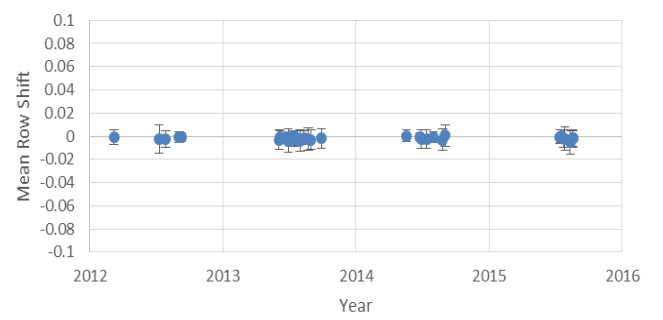M8 vs. M10 across all aggregation zones

Fig. 12. Trend plots for the on-orbit measured mean column shifts for the 3x1, 2x1 and no aggregation zones and for the on-orbit measures mean row shifts across all aggregation zones for bands M8 versus M10.
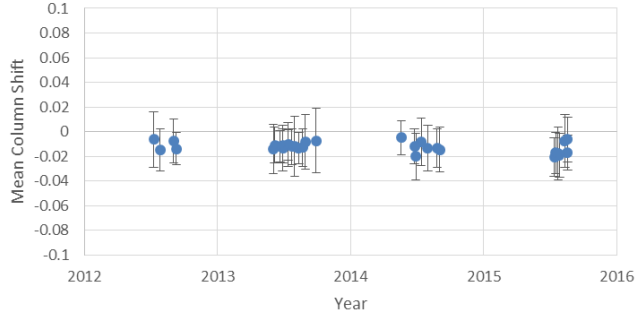
(a)

(b)

(c)
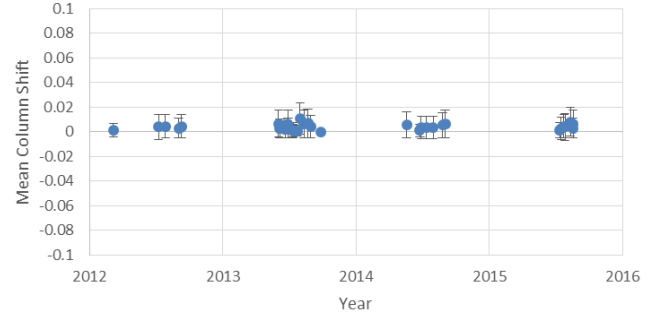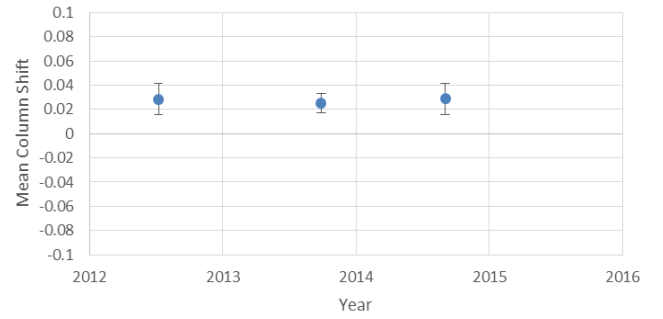
(d)

Fig. 13. Trend plots for the on-orbit measured mean column shifts for the 3x1, 2x1 and no aggregation zones and for the on-orbit measure mean row shifts across all aggregation zones for bands M12 versus M15.

Fig. 14. Trend plots for the on-orbit measured mean column shifts for the 3x1, 2x1 and no aggregation zones and for the on-orbit measure mean row shifts across all aggregation zones for bands M14 versus M16.

[9] Y. Xie, X. Xiong, J. J. Qu, N. Che and M. E. Summers, "Impact analysis of MODIS band-to-band registration on its measurements and science data products," *Int'l Journal of Remote Sens.,* vol. 32, no. 16, pp. 4431-4444, 2011.
[10] J. P. Kern and M. S. Pattichis, "Robust multispectral image registration using mutual-information models," *IEEE Trans. Geosci. Remote Sens*., vol. 45, no. 5, pp. 1494-1505, 2007.
[11] C. Studholme, D. L. G. Hill and D. Hawkes, "An overlap invariant entropy measure of 3D medical image alignment," *Pattern Recognition*, vol. 32, no. 1, pp. 71-86, 1999.
[12] K. I. Joy, "Catmull-Rom splines," *On-Line Geometric Modeling Notes*, (http://graphics.cs.ucdavis.edu/~joy/ecs278/notes/Catmull-Rom-Spline.pdf, last accessed Sep. 15, 2015).
[13] E. Catmull and R. Rom, "A class of local interpolating splines," in *Computer Aided Geometric Design*, R. E. Barnhill and R. F. Riesenfled, eds., New York: Academic Press, 1974.

James C. Tilton (S'79-M'81-SM'94) received B.A. degrees in electronic engineering, environmental science and engineering, and anthropology and a M. E. E. (electrical engineering) from Rice University, Houston, TX in 1976. He also received an M. S. in optical sciences from the University of Arizona, Tucson, AZ in 1978 and a Ph. D. in electrical engineering from Purdue University, West Lafayette, IN in 1981.

He is currently a Computer Engineer with the Computational and Information Sciences and Technology Office (CISTO) of the Science and Exploration Directorate at the NASA Goddard Space Flight Center, Greenbelt, MD. As a member of CISTO, Dr. Tilton is responsible for designing and developing computer software tools for space and earth science image analysis, and encouraging the use of these computer tools through interactions with space and Earth scientists. His software development has resulted in three patents. He has held similar positions at NASA Goddard since 1985.

Dr. Tilton is a senior member of the IEEE Geoscience and Remote Sensing Society (GRSS). From 1992 through 1996, he served as a member of the IEEE GRSS Administrative Committee. Since 1996 he has served as an Associate Editor for the IEEE Transactions on Geoscience and Remote Sensing.

Bin Tan received the B.S. degree in geography and the M.S. degree in remote sensing and GIS from Peking University, Beijing, China, in 1998 and 2001, respectively, and the Ph.D. degree in geography from Boston University, Boston, MA, 2005.

From 2005 to 2007, he was a research associate with the Department of Geography, Boston University. Dr. Tan joined the NASA Goddard Space Flight Center, Greenbelt, MD, as a contractor in 2007. His recent research interests include temporal data analysis, modeling the land cover change with high resolution satellite data, and the co-registration of remote sensing images.

Guoqing (Gary) Lin received a B.S. degree in hydro-electrical engineering from Hohai (Rivers and Oceans) University in China in 1983, an M.S. degree in Physical Oceanography from North Carolina State University in 1992, and a Ph.D. degree in Civil Engineering from University at Buffalo in 1998.

Dr. Lin joined the NASA Goddard Space Flight Center, Greenbelt, MD, as a contractor in 2006. He first supported the GOES-R Program Definition and Risk Reduction, and then supported pre-launch and on-orbit geometric calibration for the Visible Infrared Imaging Radiometer Suite (VIIRS) instruments onboard the Suomi National Polar-orbiting Partnership (SNPP) satellite and the future Joint Polar Satellite System (JPSS) satellites. His research interests include optical performance of space-borne instruments, image co-registration and satellite navigation and pointing, and their impacts on remote sensing data retrievals.